

---

# Visual Navigation by Generating Next Expected Observations

---

Qiaoyun Wu<sup>1,2</sup>, Dinesh Manocha<sup>2</sup>, Jun Wang<sup>1</sup> and Kai Xu <sup>\*3</sup>

<sup>1</sup>Nanjing University of Aeronautics and Astronautics, Nanjing, 210016

<sup>2</sup>University of Maryland, College Park, MD 20742

<sup>3</sup>National University of Defense Technology, Changsha, 410073

## Abstract

We propose a novel approach to visual navigation in unknown environments where the agent is guided by conceiving the next observations it expects to see after taking the next best action. This is achieved by learning a variational Bayesian model that *generates* the next expected observations (NEO) conditioned on the current observations of the agent and the target view. Our approach predicts the next best action based on the current observation and NEO. Our generative model is learned through optimizing a variational objective encompassing two key designs. First, the latent distribution is conditioned on current observations and target view, supporting model-based, target-driven navigation. Second, the latent space is modeled with a Mixture of Gaussians conditioned on the current observation and next best action. Our use of mixture-of-posteriors prior effectively alleviates the issue of over-regularized latent space, thus facilitating model generalization in novel scenes. Moreover, the NEO generation models the forward dynamics of the agent-environment interaction, which improves the quality of approximate inference and hence benefits data efficiency. We have conducted extensive evaluations on both real-world and synthetic benchmarks, and show that our model outperforms the state-of-the-art RL-based methods significantly in terms of success rate, data efficiency, and cross-scene generalization.

## 1 Introduction

Mapless visual navigation is an important problem for robots operating in unknown, unstructured environments. It can be generally characterized as the ability of a robot to navigate itself from an arbitrary location to a designated goal solely based on the visual inputs from its on-board sensors. Recent years have witnessed the rapid advancement of visual navigation due to deep reinforcement learning (DRL) [33, 34, 7, 25]. Model-free DRL learns to directly map raw observations to values or actions, which suffers from low data efficiency. Model-based approaches aim to address this issue through modeling the environment based on past experience. Such a model can be used to reason about the future, thus relieving the trial-and-error learning endeavor. However, it is difficult to learn a powerful model that generalizes across different scenes, a.k.a. the model imperfection issue.

We propose a model-based (non-RL) approach to visual navigation with strong model generality, where the agent is guided by conceiving the next observations it expects to see after taking the next best action. This is realized by learning a *generative model* conditioned on the multi-view observations at the current location as well as the target view, from which the next expected observation (NEO) can be generated. We predict the next best action based on the generated NEO and the current (front-view) observation. We frame this problem as a variational Bayesian inference where the variational lower-bound (objective) consists of three terms: reconstruction, regularization and classification. The

---

\*Corresponding author: kevin.kai.xu@gmail.com

minimization of the reconstruction error maximizes the likelihood of the NEO, given the current observations and target view. The regularization term drives the variational posterior to match a prior distribution. The classification term is devised for action prediction.

A key aspect of our approach is modeling of the latent space. First, to enable target-driven navigation, the latent distribution is conditioned on current observations and target view. Second, we model the latent space with a Mixture of Gaussians conditioned on current observations and next best actions. Such variational *mixture of posteriors* prior [30] effectively alleviates over-regularization of the latent space, thus facilitating cross-scene model generalization. Moreover, the NEO generation via sampling the latent space essentially models the *forward dynamics* of the agent-environment interaction, i.e., action-driven state transition. This improves the expressiveness of the approximation of variational inference [3], thereby greatly enhancing inference generalization and data efficiency.

To summarize our contributions: We propose a new model-based approach to visual navigation, where the internal model is used to reason about the next observations the agent expects to see after taking the next best action. Two key designs ensures both data efficiency and model generality. We conducted extensive evaluation on public datasets of both real-world and synthetic scenes, including the Active Vision Dataset [1] and the AI2-THOR framework [34]. We demonstrate that our model attains at least 10% and 5% higher success rate for cross-target and cross-scene generalization, respectively, compared to several state-of-the-art alternative methods. These alternatives range from model-based to model-free, from RL-based to supervised-learning-based, and from target-driven to semantic-driven. *Our source code has been submitted and will be made publicly available.*

## 2 Related Works

**Model-free navigation.** Model-free approach trains the agent by directly mapping raw observations into actions. Mnih et al. [17, 18] present the first deep reinforcement learning model which successfully learns control policies directly from high-dimensional sensory input. The model is a convolutional neural network trained with a variant of Q-learning, named Deep Q-Learning (DQN). Schulman et al. [27] proposes the Trust Region Policy Optimization (TRPO), which is effective for optimizing large nonlinear policies and demonstrates robust performance on a wide variety of robotic tasks. Lillicrap et al. [13] present the DDPG (Deep Deterministic Policy Gradient), which can robustly solve many simulated tasks. Asynchronous DQN [16] shows good performance on exploration in a 3D labyrinth. Model-free methods usually requires large amount of training data and the resulting policies do not readily generalize to novel tasks in unseen environment.

Several works study using deep neural networks to realize classical iterative planning algorithms without an explicit environment model [29, 28, 22, 11]. Zhang et al. [33] focus on the problem of robot navigation in real maze-like environments and present a successor-feature-based deep RL algorithm that can transfer navigation policies across similar environments. These models demonstrate superior performance mainly on maze-like environments rather than real-world indoor scenes.

Zhu et al. [34] propose an excellent feed-forward architecture for target-driven visual navigation by combining a Siamese network with the A3C algorithm [16]. They focus on smaller indoor scenes and does not consider generalization to previously unseen environments. In [19], semantic scene segmentation is incorporated in learning to map from semantic information to navigation actions. In the experiment, our method is compared with the two methods and demonstrates better performance.

**Model-based navigation.** Model-based navigation achieves better data efficiency, but has the issues of cross-scene generalization due to model imperfections. Several approaches has been proposed to address the model imperfection issue, such as capturing model uncertainty [4, 14] and incorporating semantic priors into environment models [32, 19]. With the advances of attention mechanism in deep learning, many works propose to model the environment with a memory unit. Oh et al. [20] propose a memory-based deep RL architecture where memory units are used for integrating (write) observation and retrieving (read) useful information for navigation. Savinov et al. [26] introduce a topological landmark-based memory for navigation. A common issue of such approach is that the memory, representing an allocentric map of the scene, grows in size as the scene exploration proceeds, limiting its practical utility in navigating within large environments. In [7], the problem is alleviated by learning an ego-centric mapper and planner, which, however, assumes perfect odometry. Henriques and Vedaldi [8] develop a differentiable module that is able to associate an egocentric representation of a scene to an allocentric one. Our method models the environment with the probabilistic latent

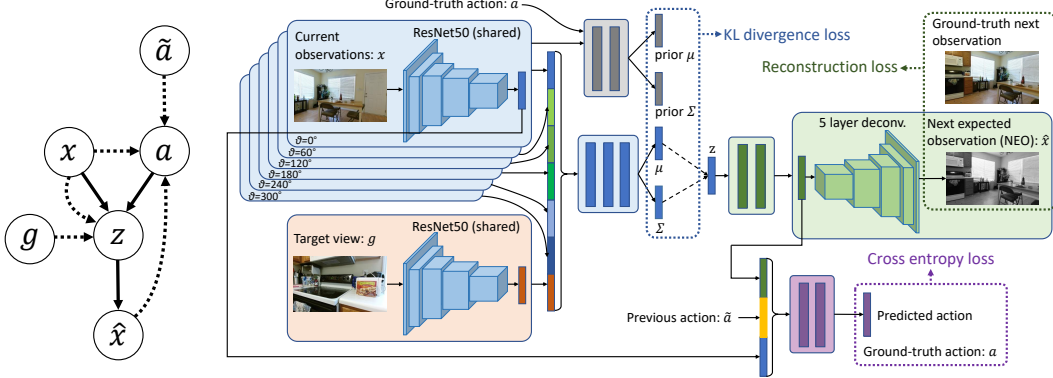


Figure 1: Model overview: the probabilistic graphical model and the network architecture. In graphical model, the posterior  $p_\theta(z|x, a)$  and generator  $p_\theta(\hat{x}|z)$  are denoted with solid lines, while the variational approximation  $q_\lambda(z|x, g)$  and the action prediction  $q_\varphi(a|x, \hat{x}, \tilde{a})$  are depicted with dashed lines. The generative model is implemented with an auto-encoder architecture: The encoder takes the current observations  $x$  and the target view  $g$  as input. The decoder generates the NEO  $\hat{x}$  from a random vector sampled from the latent space, from which the feature map is used in predicting the next action. Three losses used for learning the generative model are marked with dashed boxes.

distribution in a variational Bayesian framework, where both model generality and model scalability are attained by imposing a mixture-of-posteriors prior.

**Imagination-based navigation.** Some model-based methods conduct navigation through reasoning about the future based on the internal model. Razvan et al. [23] introduce imagination-based planner, which is the first model-based, sequential decision-making agent that can learn to propose (imagine), evaluate, and execute plans. The method demonstrates good performance on 2D maze-solving tasks. Later, Imagination-Augmented Agents (I2As) [25] is proposed which learns to generate and interpret predictions as additional context for deep policy networks. These methods are generally data-efficient, but have difficulty in scaling to complex, high-dimensional tasks. Generally, similar ideas have been well practiced in the studies of deep RL, where the internal model is used to predict future observations and/or rewards [21, 12, 5, 9, 15, 6, 24]. Watter et al. [31] introduce Embed to Control (E2C), which learns to generate image trajectories from a latent space in which the dynamics is constrained to be locally linear, in contrast to the non-linear dynamics modeled by our latent space.

Although sharing similar spirit, our work is significantly different from the imagination-augmented RL-based navigation [25, 23]. First, our model is formulated as a variational Bayesian inference which is trained with supervised learning rather than RL. Second, their imaginations refer to simulated rollout of trajectories, while our imagination is a one-step imagination of the next observation.

### 3 Method

#### 3.1 Problem setting

The target-driven visual navigation takes the current observations  $x$  captured by the agent and a target view  $g$  as input, and predicts the next best action  $a$  at each time step to navigate the agent, until reaching a location within a threshold distance to the target position.

**Observations and goals.** The agent camera has only the azimuth DoF. At each agent location, the observation  $x$  consists of  $K$  views with evenly distributed azimuth angles:  $\{0^\circ, \frac{1}{K}360^\circ, \dots, \frac{K-1}{K}360^\circ\}$ , in which  $0^\circ$  corresponds to the front-looking view. The agent captures for each view an RGB image (optionally with depth channel). The  $K$ -view observations provide a local context of the environment, based on which the agent is able to reason about its location and the room layout of its surrounding. The target view is consistent with the observation views in terms of image data modality.

**Actions space.** At each time step, the agent can choose one action from a discrete set of allowable actions:  $\{\text{move\_forward}, \text{move\_back}, \text{move\_left}, \text{move\_right}, \text{rotate\_ccw}, \text{rotate\_cw}, \text{stop}\}$ , where *move* means horizontal movement of the agent and *rotate* refers to azimuth rotation of

the camera. *ccw* and *cw* stands for counter-clockwise and clockwise, respectively. If there is no next observation view associated with an action, the action is considered to cause a collision.

### 3.2 The variational Bayesian navigation model

Given the current observation  $x$ , instead of directly predicting the next best action  $a$  like in many other works, we opt to first *generate* the next expected observation (NEO)  $\hat{x}$  assuming that the next best action  $a$  is known *a priori* and is executed. This can be described with a generative model:

$$p_\theta(\hat{x}, z|x, a) = p_\theta(\hat{x}|z)p_\theta(z|x, a), \quad (1)$$

where  $p_\theta(\hat{x}, z|x, a)$  is a parametric model of the joint distribution over the NEO  $\hat{x}$  and a latent variable  $z$ . Essentially, this generative model is a probabilistic *forward dynamics model* of the agent, where the acquirement of the next observation is driven by the current action.

To learn the generative model, one typically maximizes the marginal log-likelihood  $\log p_\theta(\hat{x}|x, a)$ . However, when the model is parameterized by a neural network, the optimization could be difficult due to the intractability of the marginal likelihood. Moreover, the next best action  $a$  is unknown *a priori* and is inherently determined by the target  $g$ . To overcome these issues, we apply *variational inference* and introduce an inference network  $q_\lambda(z|x, g)$  with parameters  $\lambda$  to approximate the true posterior  $p_\theta(z|x, a)$ . In particular, we optimize the following lower bound of the marginal likelihood:

$$\log p_\theta(\hat{x}|x, a) \geq \mathbb{E}_{z \sim q_\lambda(z|x, g)} [\log \frac{p_\theta(\hat{x}, z|x, a)}{q_\lambda(z|x, g)}] = \mathcal{L}(\hat{x}). \quad (2)$$

This lower bound forms our objective function:

$$\mathcal{J} = -\mathbb{E}_{z \sim q_\lambda(z|x, g)} [\log p_\theta(\hat{x}|z)] + KL[q_\lambda(z|x, g) || p_\theta(z|x, a)] = -\mathcal{L}(\hat{x}), \quad (3)$$

where  $KL$  denotes the Kullback-Leibler divergence. During training,  $p_\theta(z|x, a)$  can be estimated as a Gaussian distribution conditioned on the current observation  $x$  and the ground-truth action  $a$ , leading to a mixture-of-posteriors prior imposed on the latent distribution.

To realize robot navigation, we learn a navigation action classifier  $q_\varphi(a|x, \hat{x}, \tilde{a})$  which predicts the next best action  $a$  based on the current observation  $x$ , the generated NEO  $\hat{x}$  as well as the previous action  $\tilde{a}$ . Integrating action prediction, the objective function becomes:

$$\mathcal{J} = -\alpha \mathbb{E}_{z \sim q_\lambda(z|x, g)} [\log p_\theta(\hat{x}|z)] + \beta KL[q_\lambda(z|x, g) || p_\theta(z|x, a)] + \gamma \mathbb{E}_{a \sim p(a)} [-\log q_\varphi(a|x, \hat{x}, \tilde{a})] \quad (4)$$

where  $a \sim Cat(1/C)$ . A complete derivation is given in the supplementary material. Figure 1(left) shows the probabilistic graphical model of our navigation model. The objective function in (4) is composed of as a reconstruction loss, a KL divergence loss and a cross entropy loss. The three hyper-parameters are empirically set as  $\alpha = 0.01$ ,  $\beta = 0.0001$  and  $\gamma = 1$  throughout our experiments.

### 3.3 The network architecture

In accordance to the variational objective, the architecture of our network consists of three subnetworks (see Figure 1). The *variational inference module* takes the full observation views at the current robot position as well as the target view as input and extracts a 2048-D feature vector for each of them using a ResNet-50. The input image resolution is  $64 \times 64$ . These output 2048-D feature vectors are then used to infer a vector of latent variables of dimension 400 with a MLP. Here, a KL divergence loss is minimized to impose the distribution of the latent variables to match a prior estimated from the current observation (front view only) and the ground-truth action. The *NEO generation module* then generates the NEO in front view out of a latent vector, using a two-layer MLP followed by a 5-layer convolutional network (see supplementary material for details). This task is trained with supervision of ground-truth next observation. The *action prediction module* maps the concatenation of the last layer feature of the NEO generation module (2048-D), the feature of current observation (2048-D) and the feature (1024-D) extracted from the previous action (7-D one-hot vector) into the predicted next action (7-D), using a four-layer MLP. Ground-truth actions are used to train this subnetwork.

**Model training and testing.** Our model is trained and tested with both real-world environments from the Active Vision Dataset (AVD) [1] and the synthetic scenes from the AI2-THOR framework [34]. Each scene in the dataset is represented as a grid of robot locations (see Figure 4). The size of grid

cell is 0.25~0.5 meters. For each grid point, 6 azimuth camera views are captured for AVD and 4 for AI2-THOR. For the task of target-driven navigation, the ground-truth navigation path is simply the shortest path over the grid. The optimization of the variational objective is achieved by Monte Carlo sampling, where the gradients are backpropagated with the standard reparameterization trick [10].

At test time, our model is used as a controller for the agent which predicts the next action given the current observations. We feed the current observation views and the target view into the inference module to obtain a Gaussian component in the latent space. A random code is then sampled from the Gaussian for next action prediction. The actual generation of NEO is not needed during test.

## 4 Experiments

We evaluate both cross-target and cross-scene generalization of our model through comparing with one baseline and a few state-of-the-art methods. We also compare to two ablated variants of our method to justify our major design choices. In addition, we visualize the latent space for a better understanding of what we learn, as well as the navigation paths for a qualitative evaluation.

**Experimental settings.** The evaluations are conducted both on the AVD and the AI2-THOR datasets. AVD contains 11 relatively complex real-world houses, from which 8 houses were used for training and 3 for testing. AI2-THOR contains 120 scenes in four categories including kitchen, living room, bedroom, and bathroom. Each category includes 30 scenes, among which 20 are used for training and 10 for testing. For each training scene, we choose five different views as the target, each of which contains a targeted object such as a dining table, a refrigerator, a sofa, a television, a bicycle, a kitchen tap, etc. During test, the target views are randomly sampled from the test scenes, encompassing both similar to trained targets and totally unseen in training. The maximum distance from a starting point to a goal is 35 steps. In our evaluation, the agent runs up to 50 steps, unless the early stop criteria are met, i.e., the distance to goal is smaller than a threshold or a *stop* action is predicted.

We adopt two evaluation metrics, success rate and success weighted by (normalized inverse) path length (SPL) proposed in [2]. Success rate is the fraction of the runs that ends within 5 steps to the goal. SPL considers both success rate and the path length traveled:  $\frac{1}{N} \sum_{i=1}^N S_i \frac{L_i}{\max\{P_i, L_i\}}$ , where  $N$  is the number of navigation tasks,  $S_i$  a binary indicator of success in the  $i$ -th task.  $P_i$  and  $L_i$  denote the actual path length and the shortest path distance for the  $i$ -th task, respectively.

Our model is compared with the following baselines/alternatives:

- **Random Walk**, a baseline where the agent randomly chooses an action at each time step.
- **TD-A3C**, a state-of-the-art target-driven visual navigation model based on deep RL [34]. It takes first-person view images as input and adopts the A3C algorithm for policy network optimization. The scene-specific branch was not used for the category-agnostic AVD houses.
- **I2A**, short for Imagination-Augmented Agents [25], which is an imagination-based deep RL model. The original method is developed only for 2D maze-solving tasks; we re-implemented it for visual navigation task by changing its input to first-person views.
- **TD-Semantic**, a state-of-the-art target-driven navigation model based on deep supervised learning. The method leverages the semantic and contextual representations obtained by off-the-shelf object detection and segmentation methods [19].
- **Ours-NoGen**, a non-generative variant of our model where the next expected observation is predicted directly from the input of current observations and target view. This is implemented simply by disabling the KL-loss in Eq. (4).
- **Ours-NoMoP**, a baseline variant of our model in which the latent space follows the standard normal distribution prior, instead of the mixture-of-posteriors prior.

By default, all methods take RGB images as input observation. For I2A and our model, we also implemented variants taking depth and/or RGBD images as input.

**Cross-target generalization.** Over the 8 training scenes of AVD, we evaluate navigation performance for 40 novel targets unseen in the training phase. These targets are classified into five intervals of the shortest distance between the test and the nearest trained targets: [2, 3], [4, 5], [6, 7], [11, 13], and [14, 16]. For each interval, we sample 1000 navigation tasks with different starting points. The results

Table 1: Navigation performance (success rate and SPL, in %) comparison for novel targets. **Green** and **red** highlight the best numbers for RGB input only and for with depth input, respectively.

Model \ Interval	[2, 3]	[4, 5]	[6, 7]	[11, 13]	[14, 16]	Avg.
Random Walk	43.9 / 29.8	42.3 / 28.0	37.5 / 22.6	31.5 / 19.2	39.7 / 24.5	39.0 / 24.8
TD-A3C	<b>61.6</b> / 37.4	53.7 / 34.5	44.4 / 24.0	31.2 / 15.9	32.0 / 18.9	44.6 / 26.1
I2A (RGB)	47.7 / 31.5	40.9 / 27.8	38.3 / 25.3	35.0 / 20.2	39.7 / 26.0	40.3 / 26.2
Ours-NoGen	52.1 / <b>51.5</b>	55.5 / 54.6	44.3 / <b>43.7</b>	28.4 / 28.2	34.5 / 33.6	43.0 / 42.3
Ours-NoMoP	47.1 / 46.1	57.5 / 53.0	41.4 / 39.7	29.7 / 27.6	31.2 / 30.4	41.4 / 39.4
Ours (RGB)	51.8 / 49.4	<b>86.0</b> / <b>77.4</b>	<b>45.6</b> / 43.3	<b>50.5</b> / <b>43.7</b>	41.1 / <b>36.2</b>	<b>55.0</b> / <b>50.0</b>
I2A (Depth)	49.3 / 32.7	44.6 / 28.1	41.2 / 25.9	35.2 / 20.7	45.1 / 28.5	43.1 / 27.2
Ours (Depth)	<b>89.2</b> / 81.4	74.3 / 65.4	46.4 / 40.5	<b>72.0</b> / <b>59.2</b>	<b>45.3</b> / <b>40.0</b>	65.4 / 57.3
Ours (RGBD)	86.4 / <b>82.8</b>	<b>82.3</b> / <b>71.7</b>	<b>60.6</b> / <b>53.8</b>	56.7 / 45.9	41.8 / 35.7	<b>65.6</b> / <b>58.0</b>

Table 2: Navigation performance (success rate and SPL, in %) comparison on novel scenes.

Target \ Model	Table	Exit	Couch	Refrigerator	Sink	Avg.
Random Walk	57.9 / 35.8	48.6 / 31.4	48.5 / 30.8	44.9 / 28.9	31.4 / 19.2	46.3 / 29.2
TD-A3C	<b>63.2</b> / 37.4	48.5 / 27.9	48.1 / 25.8	44.5 / 24.7	34.0 / 18.7	47.7 / 26.9
I2A (RGB)	59.9 / 39.4	47.1 / 30.1	46.6 / 29.6	44.5 / 28.9	31.4 / 20.3	45.9 / 29.7
Ours-NoGen	46.9 / 42.7	33.6 / 32.4	35.4 / 33.5	39.4 / 29.4	31.2 / 27.7	37.3 / 33.1
Ours-NoMoP	54.6 / 42.1	48.9 / <b>40.6</b>	<b>48.9</b> / <b>40.3</b>	36.0 / 28.8	27.6 / 22.3	43.2 / 34.8
Ours (RGB)	62.0 / <b>48.6</b>	<b>51.4</b> / 40.0	48.5 / 38.7	<b>48.5</b> / <b>35.5</b>	<b>45.1</b> / <b>32.5</b>	<b>51.1</b> / <b>39.1</b>
I2A (Depth)	61.0 / 39.3	50.0 / 33.5	50.4 / 33.7	49.0 / 30.7	36.0 / 22.7	49.3 / 22.7
Ours (Depth)	73.8 / <b>61.7</b>	<b>83.1</b> / <b>57.4</b>	<b>73.3</b> / <b>48.5</b>	<b>59.3</b> / <b>46.0</b>	<b>44.6</b> / <b>34.5</b>	<b>66.8</b> / <b>49.6</b>
Ours (RGBD)	<b>76.3</b> / 54.8	60.9 / 44.5	53.2 / 40.8	55.6 / 37.4	43.5 / 31.3	57.9 / 41.8

on the two metrics are reported in Table 1. Generally, the success rate decreases as the distance between the test and trained targets increases. Our model with default RGB input outperforms the state-of-the-art alternatives by > 10% for success rate and by > 20% for SPL. An observation is that the success rate is related to the presence of targeted object in the target views. If the targeted object is completely visible in the target view, the target is more instructive and thus easier to reach. The results by reversing the start and target points can be found in the supplementary material.

**Cross-scene generalization.** To evaluate model generality over unseen scenes, we perform navigation with randomly chosen 15 target views from the testing split of AVD. The targets are classified into five groups according to the object of interest in the target views; see Table 2. Note object labels were not used for navigation. For each group, we randomly sample 1000 navigation tasks (starting points). Our model achieves  $\sim 5\%$  higher average success rate and  $> 10\%$  higher average SPL than the alternative methods. The plot in Figure 2(left) compares average success rate of different models over increasing number of time steps, tested on AVD. Our method leads to steeper curves than TD-A3C and I2A for RGB input, and achieves the steepest increase when depth channel is used.

Table 3 evaluates target-driven navigation over synthetic scenes from AI2-THOR. For each of the four room categories, 1000 randomly generated navigation tasks are sampled from the testing split of the dataset. All methods being compared take RGB input. The success criterion is set to within 2 steps to the goal, due to the smaller room size in the dataset. The random walk baseline can be used as a reference to assess the difficulty of the navigation tasks. For example, the living rooms are more challenging since all methods perform poorly while the bathrooms are relatively easier. For bathroom, however, our method fails to beat the baselines, because the transparent glass and texture-less furniture make it hard for our model to infer the surrounding layout which is important to NEO imagination and action prediction. Overall, our model has much better cross-scene generality.

Table 3: Comparing navigation performance (success rate and SPL) on novel scenes from AI2-THOR.

Model \ Category	Kitchen	Living room	Bedroom	Bathroom	Avg.
Random Walk	39.2 / 17.1	16.2 / 6.9	31.8 / 12.9	<b>68.8</b> / <b>38.0</b>	39.0 / 18.7
TD-A3C	37.4 / 15.8	14.3 / 6.3	26.1 / 10.7	<b>68.8</b> / 35.1	36.7 / 17.0
I2A	40.3 / 17.6	13.4 / 5.3	30.4 / 13.0	63.0 / 32.4	36.8 / 17.1
Ours	<b>62.7</b> / <b>39.3</b>	<b>25.5</b> / <b>13.1</b>	<b>58.6</b> / <b>36.8</b>	55.3 / 36.9	<b>50.5</b> / <b>31.5</b>

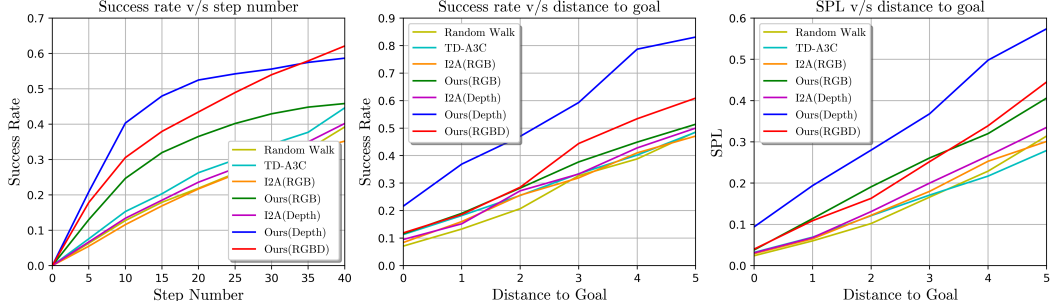


Figure 2: We report the success rate (left and middle) and the SPL (right) over number of time steps or distance to goal for different models. Each curve is measured based on 1000 navigation tasks.

Table 4: Performance (success rate) comparison of semantic-driven navigation.

Model \ Target label	Couch	Table	Refrigerator	Microwave	TV	Avg.
TD-Semantic (Object)	80.0	38.0	68.0	38.0	44.0	53.6
Ours (RGB)	64.7	73.7	61.3	38.7	31.3	53.9
Ours (Depth)	<b>83.4</b>	67.4	57.8	41.1	<b>82.0</b>	<b>66.3</b>
Ours (RGBD)	73.5	<b>83.5</b>	<b>72.1</b>	<b>41.5</b>	11.8	56.4

**Ablation study.** Tables 1 and 2 also provide an ablation study. From the comparison with NoGen, our generative method performs much better than the non-generative version, under the same amount of training. This confirms the consensus that model-based approaches are generally more data-efficient than model-free ones. Furthermore, the comparison to NoMoP shows that our carefully designed mixture-of-posterior prior leads to more powerful internal model through overcoming the over-regularization of latent space caused by the commonly used standard normal distribution prior.

**Input modality.** Through comparison on different input modalities (Tables 1 and 2), the conclusion is that depth information is apparently more useful to our model. This is because depth images contain rich geometry information which helps our agent learns a powerful inference model for reasoning about the surrounding layout and for modeling the action-observation dynamics.

**Close-to-goal stability.** In most navigation methods, the agent’s path tends to oscillate when the agent gets close to the goal. The main reason is that the situations that the agent is close to the goal is generally sparse in training. This leads to imbalanced positive and negative situations in training data. Therefore, it is hard for the trained agent to make a *stop* decision precisely and decisively when approaching the goal. Figure 2(middle and right) plot the success rate and SPL over varying values of distance-to-goal threshold used for judging navigation success. In general, smaller thresholds lead to lower success rate due to higher chance of close-to-goal oscillation. The plots show that our method achieves more stable close-to-goal convergence for all thresholds, thanks to the expressive approximation of variational inference learned through modeling the agent-environment interaction. The latter leads to high data efficiency even for sparse training samples.

**Navigation driven by semantic labels.** In methods like TD-Semantic [19], the navigation goal is defined in the form of a one-hot vector over a prescribed set of semantic labels, for example,  $\{Couch, Table, Refrigerator, Microwave, TV\}$ . To compare with TD-Semantic, we adapt our method to take the same navigation goal. The comparison is conducted on AVD with the same training/testing split. TD-Semantic can learn visual representations for navigation either from RGB and/or depth input, or from semantic input of object detection and segmentation obtained by off-the-shelf state-of-the-art methods. Under the same input modality, our method outperforms TD-Semantic by 23% for RGB input, 35% for depth input, and 28% for RGBD input for average success rate. Our best performance (with depth input) is 12.7% higher than theirs with semantic input. Table 4 reports the breakdown results over various target labels for TD-Semantic with semantic input and our method with RGB and/or depth as input. We attribute the good performance to the natural design of learning task in our model. In TD-Semantic, a deep neural network is learned to predict action cost from the current observation, the goal and the previous action. In contrast, our model predicts the next observation from a latent space modeling the dynamics of action-driven observation

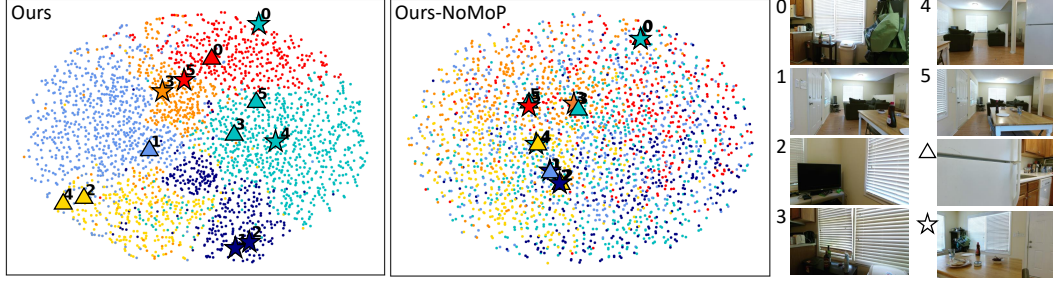


Figure 3: A t-SNE visualization of the latent space of our model (left) and its NoMoP variant (middle). The color of data points indicates action prediction. Some data points are marked with an index of the current (front-view) observation and a shape symbol indicating the target view (see the indexing of the corresponding view images to the right). The ground-truth action of a data point is visualized as the fill color of the corresponding shape symbol. Our model leads to more accurate action prediction.

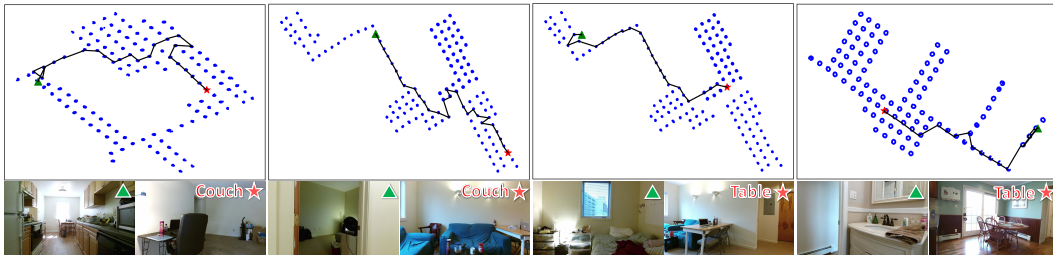


Figure 4: Visualize of navigation paths in four tasks from AVD. Blue dot represent a reachable position in the scene. Green triangles and red stars denote starting and goal points, respectively.

transition, making it easier to learn an enriched, meaningful representation (see Figure 3). Moreover, the variational inference module learns to reason about the surrounding layout based on multi-view observations, which is helpful for goal-directed decision making even if the goal is represented in an abstract form of semantic label instead of a concrete view image.

#### 4.1 Visualization

**Visualization of the latent space.** To investigate how well our latent space models the navigation policy based on the current observation and the target view, we show in Figure 3 a t-SNE visualization of the latent space learned by our model and its NoMoP baseline. There are two observations. First, the latent space by our model exhibits clear structure w.r.t. action predictions (see the color-coding), making it well suited for navigation decision making. Such expressive latent distribution is facilitated by the imposing of the mixture-of-posterior prior conditioned on current observations and next actions. In contrast, the latent space constrained by a standard Gaussian prior (NoMoP) is highly unstructured. Second, our action prediction is highly accurate (see the correspondence between data point color (action prediction) and shape symbol fill color (ground-truth action)) thanks to the action-driven variational model for NEO estimation and the separate capacity in the network of action prediction.

**Visualization of navigation paths.** In Figure 4, we visualize the agent paths for four navigation tasks in three unseen scenes from AVD. Our agent takes close to shortest paths and achieves successful navigation to the target with no prior knowledge about the environment. A visual comparison of navigation paths against alternative methods is provided in the supplementary material.

## 5 Conclusion

We have presented a generative model for visual navigation which predicts the next action based on the imagination of the next expected observation. The expressive approximation of the variational posterior as Mixture of Gaussian leads to a data-efficient model with good generality. We see great potential in incorporating this generative model into a deep RL framework to address the model imperfection issue in novel scenes, similar to the attempts made in [25].

## References

- [1] P. Ammirato, P. Poirson, E. Park, J. Košecká, and A. C. Berg. A dataset for developing and benchmarking active vision. In *2017 IEEE International Conference on Robotics and Automation (ICRA)*, pages 1378–1385. IEEE, 2017.
- [2] P. Anderson, A. Chang, D. S. Chaplot, A. Dosovitskiy, S. Gupta, V. Koltun, J. Kosecka, J. Malik, R. Motaghi, M. Savva, et al. On evaluation of embodied navigation agents. *arXiv preprint arXiv:1807.06757*, 2018.
- [3] C. Cremer, X. Li, and D. Duvenaud. Inference suboptimality in variational autoencoders. In *International Conference on Machine Learning*, 2018.
- [4] M. Deisenroth and C. E. Rasmussen. Pilco: A model-based and data-efficient approach to policy search. In *Proceedings of the 28th International Conference on machine learning (ICML-11)*, pages 465–472, 2011.
- [5] A. Dosovitskiy and V. Koltun. Learning to act by predicting the future. *arXiv preprint arXiv:1611.01779*, 2016.
- [6] C. Finn and S. Levine. Deep visual foresight for planning robot motion. In *2017 IEEE International Conference on Robotics and Automation (ICRA)*, pages 2786–2793. IEEE, 2017.
- [7] S. Gupta, J. Davidson, S. Levine, R. Sukthankar, and J. Malik. Cognitive mapping and planning for visual navigation. In *Proceedings of the IEEE Conference on Computer Vision and Pattern Recognition*, pages 2616–2625, 2017.
- [8] J. F. Henriques and A. Vedaldi. Mapnet: An allocentric spatial memory for mapping environments. In *proceedings of the IEEE Conference on Computer Vision and Pattern Recognition*, pages 8476–8484, 2018.
- [9] M. Jaderberg, V. Mnih, W. M. Czarnecki, T. Schaul, J. Z. Leibo, D. Silver, and K. Kavukcuoglu. Reinforcement learning with unsupervised auxiliary tasks. *arXiv preprint arXiv:1611.05397*, 2016.
- [10] D. P. Kingma and M. Welling. Auto-encoding variational bayes. *arXiv preprint arXiv:1312.6114*, 2013.
- [11] L. Lee, E. Parisotto, D. S. Chaplot, E. Xing, and R. Salakhutdinov. Gated path planning networks. *arXiv preprint arXiv:1806.06408*, 2018.
- [12] F. Leibfried, N. Kushman, and K. Hofmann. A deep learning approach for joint video frame and reward prediction in atari games. *arXiv preprint arXiv:1611.07078*, 2016.
- [13] T. P. Lillicrap, J. J. Hunt, A. Pritzel, N. Heess, T. Erez, Y. Tassa, D. Silver, and D. Wierstra. Continuous control with deep reinforcement learning. *arXiv preprint arXiv:1509.02971*, 2015.
- [14] A. Marco, F. Berkenkamp, P. Hennig, A. P. Schoellig, A. Krause, S. Schaal, and S. Trimpe. Virtual vs. real: Trading off simulations and physical experiments in reinforcement learning with bayesian optimization. In *2017 IEEE International Conference on Robotics and Automation (ICRA)*, pages 1557–1563. IEEE, 2017.
- [15] P. Mirowski, R. Pascanu, F. Viola, H. Soyer, A. J. Ballard, A. Banino, M. Denil, R. Goroshin, L. Sifre, K. Kavukcuoglu, et al. Learning to navigate in complex environments. *arXiv preprint arXiv:1611.03673*, 2016.
- [16] V. Mnih, A. P. Badia, M. Mirza, A. Graves, T. Lillicrap, T. Harley, D. Silver, and K. Kavukcuoglu. Asynchronous methods for deep reinforcement learning. In *International conference on machine learning*, pages 1928–1937, 2016.
- [17] V. Mnih, K. Kavukcuoglu, D. Silver, A. Graves, I. Antonoglou, D. Wierstra, and M. Riedmiller. Playing atari with deep reinforcement learning. *arXiv preprint arXiv:1312.5602*, 2013.
- [18] V. Mnih, K. Kavukcuoglu, D. Silver, A. A. Rusu, J. Veness, M. G. Bellemare, A. Graves, M. Riedmiller, A. K. Fidjeland, G. Ostrovski, et al. Human-level control through deep reinforcement learning. *Nature*, 518(7540):529, 2015.
- [19] A. Mousavian, A. Toshev, M. Fiser, J. Kosecka, and J. Davidson. Visual representations for semantic target driven navigation. *arXiv preprint arXiv:1805.06066*, 2018.
- [20] J. Oh, V. Chockalingam, S. Singh, and H. Lee. Control of memory, active perception, and action in minecraft. *arXiv preprint arXiv:1605.09128*, 2016.
- [21] J. Oh, X. Guo, H. Lee, R. L. Lewis, and S. Singh. Action-conditional video prediction using deep networks in atari games. In *Advances in neural information processing systems*, pages 2863–2871, 2015.
- [22] J. Oh, S. Singh, and H. Lee. Value prediction network. In *Advances in Neural Information Processing Systems*, pages 6118–6128, 2017.
- [23] R. Pascanu, Y. Li, O. Vinyals, N. Heess, L. Buesing, S. Racanière, D. Reichert, T. Weber, D. Wierstra, and P. Battaglia. Learning model-based planning from scratch. *arXiv preprint arXiv:1707.06170*, 2017.
- [24] D. Pathak, P. Agrawal, A. A. Efros, and T. Darrell. Curiosity-driven exploration by self-supervised prediction. In *Proceedings of the IEEE Conference on Computer Vision and Pattern Recognition Workshops*, pages 16–17, 2017.
- [25] S. Racanière, T. Weber, D. Reichert, L. Buesing, A. Guez, D. J. Rezende, A. P. Badia, O. Vinyals, N. Heess, Y. Li, et al. Imagination-augmented agents for deep reinforcement learning. In *Advances in neural information processing systems*, pages 5690–5701, 2017.
- [26] N. Savinov, A. Dosovitskiy, and V. Koltun. Semi-parametric topological memory for navigation. *arXiv preprint arXiv:1803.00653*, 2018.

- [27] J. Schulman, S. Levine, P. Abbeel, M. Jordan, and P. Moritz. Trust region policy optimization. In *International Conference on Machine Learning*, pages 1889–1897, 2015.
- [28] D. Silver, H. van Hasselt, M. Hessel, T. Schaul, A. Guez, T. Harley, G. Dulac-Arnold, D. Reichert, N. Rabinowitz, A. Barreto, et al. The predictron: End-to-end learning and planning. In *Proceedings of the 34th International Conference on Machine Learning-Volume 70*, pages 3191–3199. JMLR. org, 2017.
- [29] A. Tamar, Y. Wu, G. Thomas, S. Levine, and P. Abbeel. Value iteration networks. In *Advances in Neural Information Processing Systems*, pages 2154–2162, 2016.
- [30] J. M. Tomczak and M. Welling. Vae with a vampprior. *arXiv preprint arXiv:1705.07120*, 2017.
- [31] M. Watter, J. Springenberg, J. Boedecker, and M. Riedmiller. Embed to control: A locally linear latent dynamics model for control from raw images. In *Advances in neural information processing systems*, pages 2746–2754, 2015.
- [32] W. Yang, X. Wang, A. Farhadi, A. Gupta, and R. Mottaghi. Visual semantic navigation using scene priors. *arXiv preprint arXiv:1810.06543*, 2018.
- [33] J. Zhang, J. T. Springenberg, J. Boedecker, and W. Burgard. Deep reinforcement learning with successor features for navigation across similar environments. In *2017 IEEE/RSJ International Conference on Intelligent Robots and Systems (IROS)*, pages 2371–2378. IEEE, 2017.
- [34] Y. Zhu, R. Mottaghi, E. Kolve, J. J. Lim, A. Gupta, L. Fei-Fei, and A. Farhadi. Target-driven visual navigation in indoor scenes using deep reinforcement learning. In *2017 IEEE International Conference on Robotics and Automation (ICRA)*, pages 3357–3364, 2017.

## 6 Appendix

### 6.1 Derivation of the variational Bayesian navigation model

Given the current observation  $x$ , we opt to generate the next expected observation (NEO)  $\hat{x}$  assuming that the next best action  $a$  is known *a priori* and is executed. This can be described with a generative model:

$$p_\theta(\hat{x}, z|x, a) = p_\theta(\hat{x}|z)p_\theta(z|x, a) \quad (5)$$

We introduce a distribution  $q_\lambda(z|x, g)$  with parameters  $\lambda$  that approximates the true distribution  $p_\theta(z|x, a)$ . Then we obtain the marginal likelihood of the model:

$$\begin{aligned} \log p_\theta(\hat{x}|x, a) &= \log \int_z p_\theta(\hat{x}, z|x, a) dz \\ &= \log \int_z p_\theta(\hat{x}, z|x, a) \frac{q_\lambda(z|x, g)}{q_\lambda(z|x, g)} dz \\ &= \log E_{z \sim q_\lambda(z|x, g)} \left[ \frac{p_\theta(\hat{x}, z|x, a)}{q_\lambda(z|x, g)} \right] \\ &\geq E_{z \sim q_\lambda(z|x, g)} \left[ \log \frac{p_\theta(\hat{x}, z|x, a)}{q_\lambda(z|x, g)} \right] = \mathcal{L}(\hat{x}) \end{aligned} \quad (6)$$

To maximize the marginal likelihood, we maximize its lower bound:

$$\begin{aligned} &E_{z \sim q_\lambda(z|x, g)} \left[ \log \frac{p_\theta(\hat{x}, z|x, a)}{q_\lambda(z|x, g)} \right] \\ &= E_{z \sim q_\lambda(z|x, g)} \left[ \log \frac{p_\theta(\hat{x}|z)p_\theta(z|x, a)}{q_\lambda(z|x, g)} \right] \\ &= E_{z \sim q_\lambda(z|x, g)} \left[ \log p_\theta(\hat{x}|z) + \log \frac{p_\theta(z|x, a)}{q_\lambda(z|x, g)} \right] \\ &= E_{z \sim q_\lambda(z|x, g)} \left[ \log p_\theta(\hat{x}|z) \right] - \mathcal{KL}[q_\lambda(z|x, g) || p_\theta(z|x, a)] \end{aligned} \quad (7)$$

This lower bound forms our objective function  $-\mathcal{L}(\hat{x})$ . Further, to predict the next best action  $a$  based on the generated next expected observation  $\hat{x}$ , we train an action classifier  $q_\varphi(a|x, \hat{x}, \tilde{a})$  with  $a \sim \text{Cat}(1/C)$  and  $C$  represents the number of action labels.  $\tilde{a}$  represents the action being chosen at the previous time step. We then obtain the following extended objective function:

$$\mathcal{J} = \alpha E_{z \sim q_\lambda(z|x, g)} [-\log p_\theta(\hat{x}|z)] + \beta \mathcal{KL}[q_\lambda(z|x, g) || p_\theta(z|x, a)] + \gamma E_{a \sim p(a)} [-\log q_\varphi(a|x, \hat{x}, \tilde{a})] \quad (8)$$

where the hyper-parameter  $(\alpha, \beta, \gamma)$  tunes the relative importance of the three terms.

## 6.2 Model architecture and training details

Our navigation model consists of four modules:  $q_\lambda(z|x, g)$ ,  $p_\theta(\hat{x}|z)$ ,  $q_\varphi(a|x, \hat{x}, \tilde{a})$ , and  $p_\theta(z|x, a)$ .  $q_\lambda(z|x, g)$  first uses the ResNet-50 to extract the features of the current full observation views and the target view, followed by seven fully connected (FC) layers. The final FC layer connects to two heads to output the mean and variance of a Gaussian distribution from which our latent vector  $z$  is sampled. Given the vector  $z$ ,  $p_\theta(\hat{x}|z)$  is composed of two FC layers followed by a five-layer transposed convolutional network (see Figure 5).  $q_\varphi(a|x, \hat{x}, \tilde{a})$  is a four-layer MLP, which takes the feature of  $x$  from the ResNet-50, the feature from  $p_\theta(\hat{x}|z)$ , and the feature extracted from the previous action  $\tilde{a}$  by a FC layer as inputs, and predicts the next action for navigation.  $p_\theta(z|x, a)$  is used only in the training stage to regularize the distribution from  $q_\lambda(z|x, g)$ , taking the feature of current observation  $x$  and the ground truth next best action  $a^{gt}$  as inputs.

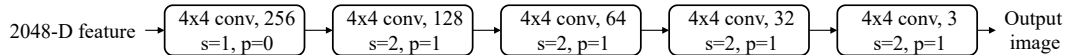


Figure 5: The 5-layer transposed convolutional network for  $p_\theta(\hat{x}|z)$ .

We can either jointly train all submodules within the architecture, or pretrain the ResNet-50 (denoted as  $f$ ) and the  $q_\varphi(a|x, \hat{x}, \tilde{a})$  submodule. In practice, we found that pre-training leads to faster training of our model. In this case, let  $f(x)$  and  $f(\hat{x}^{gt})$  represent the features from the ResNet-50, based on the input of current observation  $x$  and the ground truth next observation  $\hat{x}^{gt}$ , respectively.  $q_\varphi(a|x, \hat{x}, \tilde{a})$  takes  $f(x)$ ,  $f(\hat{x}^{gt})$ , and the feature extracted from the previous action  $\tilde{a}$  by a FC layer as inputs. The loss function for the pre-training is a classification loss  $E_{a \sim p(a)}[-\log q_\varphi(a|x, \hat{x}, \tilde{a})]$ .

We use the Stochastic Gradient Descent (SGD) optimizer, with a learning rate of  $10^{-4}$ . We terminate the training when the action prediction accuracy approaches 70%. Subsequently, we train the whole model jointly using SGD, with a learning rate of  $10^{-5}$ . The motivations of the pre-training are two folds: 1) We hope the ResNet-50 extracts more discriminative features for navigation; 2) We hope the  $q_\varphi(a|x, \hat{x}, \tilde{a})$  learns the difference between  $x$  and  $\hat{x}$  and maps the difference to a driving action from  $x$  to  $\hat{x}$ . In addition, the architecture in Figure 5 can be further simplified. We can directly use the feature after two FC layers of  $p_\theta(\hat{x}|z)$ , denoted as  $f'(\hat{x})$ , and the feature  $f(\hat{x}^{gt})$  from ResNet-50 to substitute the reconstruction term in our objective function by a  $L2$  norm without sacrificing accuracy. This simplification reduces the number of parameters and hence computational cost.

Our model is trained and tested on a PC with 12 Intel(R) Xeon(R) W-2133 CPU, 3.60 GHz and a Geforce GTX 1080 Ti GPU. The training time of our model is 20 hours for 6-view RGB or depth input, 22 hours for 6-view RGBD input. The testing time for our model is 0.03 second.

## 6.3 Additional results

**Path-reversing generalization.** This experiment is a supplement to the evaluation of cross-target and cross-scene generalization in the main paper. Here, we reverse the start and target points of each navigation task. The results are reported in Tables 5 and 6. Although most models suffer from performance degrading for path reversing tasks, our model with RGB input performs equally well compared to original tasks, and achieves higher success rate than all other methods. The performance of our model with depth input has slight performance decreasing. Therefore, although depth information can provide strong cues for room layout, such input tends to be too strong for learning a more general model.

**Data-efficiency.** We also evaluate how well our model generalizes when trained on decreasing numbers of scenes from the training split of AVD; see Table 7. The evaluation involves 1000 different navigation tasks sampled from the testing split of AVD. Different from TD-A3C, our model has a consistent trend of increasing success rate and SPL with increasing number of training scenes. For varying number of training scenes, our method, especially when using depth input, performs better than TD-A3C, demonstrating better data-efficiency.

**Cross-target generalization on AI2-THOR.** We also provide an experiment over the 80 training scenes from AI2-THOR with 240 new targets. These targets are also categorized into five intervals: [2, 3], [4, 5], [6, 7], [11, 13] and [14, 16], based on the minimum distances between these targets and their nearest trained targets. For each interval, we sample 1000 navigation tasks without repetition

Table 5: Navigation performance (success rate and SPL, in %) of cross-target generalization. **Green** and **red** highlight the best numbers for RGB input only and for with depth input, respectively.

Model \ Interval	[2, 3]	[4, 5]	[6, 7]	[11, 13]	[14, 16]	Avg.
Random Walk	46.4 / 29.5	40.1 / 25.1	37.9 / 21.6	31.7 / 18.7	38.6 / 23.8	38.9 / 23.7
TD-A3C	47.2 / 25.0	48.1 / 30.7	40.9 / 21.0	34.0 / 18.4	47.8 / 27.1	43.6 / 24.4
No-Gen	47.0 / 45.8	46.7 / 45.8	50.4 / 49.6	45.7 / <b>45.2</b>	50.1 / 48.9	48.0 / 41.1
No-MoP	49.6 / 46.7	38.9 / 36.5	47.0 / 45.1	42.4 / 40.7	54.9 / 52.8	46.6 / 44.4
I2A (RGB)	48.3 / 32.1	43.6 / 27.1	39.9 / 23.6	32.2 / 18.3	39.1 / 24.6	40.6 / 25.1
Ours (RGB)	<b>56.6 / 50.7</b>	<b>54.8 / 47.3</b>	<b>55.8 / 52.9</b>	<b>49.2 / 44.9</b>	<b>63.5 / 57.7</b>	<b>56.0 / 50.7</b>
I2A (Depth)	49.0 / 33.9	45.1 / 27.7	43.2 / 25.3	40.6 / 26.1	34.0 / 20.9	42.4 / 26.8
Ours (Depth)	<b>66.5 / 58.2</b>	57.4 / 50.5	<b>63.1 / 55.9</b>	<b>58.2 / 50.2</b>	60.9 / 54.7	61.2 / 53.9
Ours (RGBD)	63.0 / 58.1	<b>59.0 / 53.6</b>	61.6 / 55.1	55.0 / <b>50.9</b>	<b>70.4 / 64.9</b>	<b>61.8 / 56.5</b>

Table 6: Navigation performance (success rate and SPL, in %) of cross-scene generalization.

Target Models \ Scene	Table	Exit	Couch	Fridge	Sink	Avg.
Random walk	52.0 / 33.1	46.4 / 29.9	50.9 / 31.8	47.3 / 28.2	38.1 / 23.2	46.9 / 29.2
A3C	50.2 / 27.7	43.0 / 24.2	46.1 / 25.3	44.1 / 17.7	36.7 / 19.0	44.0 / 22.8
Direct NEO	37.6 / 35.9	29.1 / 26.4	30.1 / 29.0	31.3 / 28.9	22.1 / 19.3	30.0 / 27.9
Vanilla NEO	46.0 / 37.6	32.9 / 27.7	41.9 / 29.5	40.1 / 31.8	36.5 / 24.1	39.5 / 30.1
I2A (RGB)	<b>53.1 / 33.9</b>	44.4 / 29.6	46.8 / 30.6	46.5 / 28.3	37.1 / 21.8	45.6 / 38.8
Ours (RGB)	44.7 / <b>35.1</b>	<b>49.9 / 31.8</b>	<b>60.3 / 40.9</b>	<b>56.8 / 40.6</b>	<b>49.2 / 41.2</b>	<b>52.2 / 37.9</b>
I2A (Depth)	51.0 / 35.3	47.7 / 31.5	49.5 / 31.4	49.3 / 30.9	41.8 / 24.1	47.9 / 30.6
Ours (Depth)	<b>56.3 / 42.6</b>	<b>61.5 / 44.9</b>	<b>63.6 / 48.3</b>	52.1 / 39.4	<b>51.1 / 36.4</b>	<b>56.9 / 42.4</b>
Ours (RGBD)	52.0 / 40.2	58.6 / 42.1	60.4 / 44.6	56.3 / 40.5	50.7 / 37.4	55.6 / 41.0

Table 7: Performance (success rate and SPL, in %) for different number of training scenes.

Model \ # Scene	8	6	4	2
TD-A3C	48.6 / 29.4	48.2 / 28.9	49.4 / 30.0	46.6 / 26.8
Ours (RGB)	53.7 / 39.3	52.6 / 36.6	51.4 / 35.7	48.9 / 32.5
Ours (Depth)	<b>67.5 / 49.8</b>	<b>62.5 / 45.3</b>	<b>61.1 / 44.3</b>	<b>59.0 / 42.6</b>

Table 8: Navigation performance (success rate and SPL, in %) for cross-target generalization on AI2-THOR.

Model \ Interval	[2, 3]	[4, 5]	[6, 7]	[11, 13]	[14, 16]	Avg.
Random Walk	46.5 / 24.3	33.9 / 18.1	33.1 / 17.4	25.8 / 12.6	25.0 / 11.4	32.9 / 16.8
TD-A3C	43.0 / 18.9	30.9 / 13.9	30.3 / 13.4	21.7 / 10.3	22.1 / 10.2	29.6 / 13.3
Ours (RGB)	<b>75.7 / 53.7</b>	<b>67.4 / 49.0</b>	<b>51.6 / 35.0</b>	<b>31.4 / 24.3</b>	<b>30.5 / 22.8</b>	<b>51.3 / 37.0</b>

Table 9: Comparing average success rate (in %) of our model and TD-Semantic for navigation driven by semantic labels, based on various input modalities.

Ours			TD-Semantic			
RGB	Depth	RGBD	RGB	Depth	RGBD	Det.
54	66	60	31	31	28	48

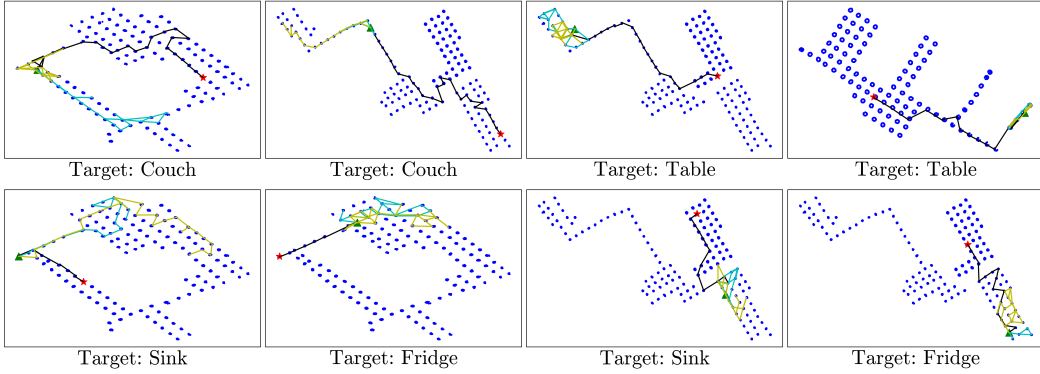


Figure 6: Visual comparison of navigation paths between our method, TD-A3C and I2A, over eight different navigation tasks. Blue dot represent a reachable position in the scene. Green triangles and red stars denote starting and goal points, respectively. I2A and TD-A3C choose the cyan and the yellow paths, respectively. Both agents fail to reach the goals. Our agent takes the black paths and is able to successfully navigate to the goals.

for evaluation. The results are presented in Table 8. We again observe that our model consistently outperforms the TD-A3C method with a large margin.

**Navigation driven by semantic labels.** We report the average performances of our method and TD-Semantic for semantic-driven navigation tasks. Both models are trained on AVD and tested on three unseen scenes. Our results are based on 2000 navigation tasks randomly sampled from the three test scenes. As shown in Table 9, our method outperforms the TD-Semantic for all input modalities.

**Visual comparison of navigation paths.** We visualize the agent trajectories by our model and two alternatives (TD-A3C and I2A), for eight different navigation tasks (see Figure 6). These are all relatively challenging tasks in which the agent starts from a location from where the desired goal is completely invisible to the agent. For all the eight tasks, both alternative methods fail to reach the goals. In contrast, our agent is able to navigate to the goals successfully.